

Main Manuscript for

Nonlocally coupled moisture model for convective self-aggregation

Tomoro Yanase^{a,b}, Shin-ichiro Shima^{c,b}, Seiya Nishizawa^b, Hirofumi Tomita^{b,a}

^aRIKEN Cluster for Pioneering Research, 7-1-26 Minatojima-minami-machi, Chuo-ku, Kobe, Hyogo 650-0047, Japan

^bRIKEN Center for Computational Science, 7-1-26 Minatojima-minamimachi, Chuo-ku, Kobe, Hyogo 650-0047, Japan

^cGraduate School of Information Science, University of Hyogo, 7-1-28 Minatojima-minamimachi, Chuo-ku, Kobe, Hyogo 650-0047, Japan

*Tomoro Yanase

Email: tomoro.yanase@riken.jp

Author Contributions: T.Y. designed research; T.Y. and S.S. performed research; T.Y. and S.S. analyzed data; and T.Y., S.S., S.N., and H.T. wrote the paper.

Competing Interest Statement: The authors declare no conflict of interest.

Classification: Physical Sciences (Major), Applied Physical Sciences (Minor)

Keywords: Moist convection | Clouds | Nonlinear dynamics | Pattern formation | Self-organization

This PDF file includes:

Main Text
Figures 1 to 4

Abstract

Clouds play a central role in climate physics by interacting with precipitation, radiation, and circulation. Although the self-aggregation of clouds is a fundamental problem in convective organization, a theoretical explanation of how it occurs has not been established owing to its complexity. Here, we introduce an idealized mathematical model of the phenomenon in which the state of the system is represented solely by the atmospheric columns' vertically integrated water vapor content. By analyzing the nonlinear dynamics of this simplified system, we mathematically elucidated the mechanisms that determine the onset of self-aggregation and the spatial scale of the self-aggregated state. Nonlocal coupling between atmospheric columns makes the system bistable with dry and moist equilibria, reflecting the effect of circulation driven by horizontal differential heating due to convection and radiation. The bistable self-aggregated state is realized when destabilization by nonlocal coupling triggered by finite-amplitude disturbances in the uniform state overwhelms the stabilization by diffusion. For globally coupled systems in which all the columns are equally coupled, the perturbation of the maximum wavelength has the maximum

growth rate. A solution with an infinitely long wavelength exists, which can be understood as the dynamical system's heteroclinic trajectories describing the steady state's spatial evolution. In contrast, for nonlocally coupled systems with finite filter lengths, perturbation of the wavelength close to the characteristic length of the coupling is preferred. The results revealed that the balance between nonlocal coupling and diffusion is essential for understanding convective self-aggregation.

Significance Statement

Cloud self-organization is a long-standing fundamental problem in climate physics, and its representation in climate models may be a source of uncertainty in future climate predictions. Clouds are complex phenomena closely intertwined with the latent heat release associated with the phase change of water, fluid motion via buoyancy, and interaction with atmospheric radiation; therefore, their elaborate modeling is underway. Attempts have also been made to understand the macroscopic behavior of clouds using a simple mathematical description. Here, we semi-analytically reveal the mechanism of the spontaneous clustering of clouds and the characteristic distances between clusters using an idealized mathematical model describing the spatiotemporal variation of water vapor content in the atmospheric columns of the tropics.

Main Text

Introduction

Clouds are central in determining Earth's climate (Siebesma et al. 2020). Among the various cloud phenomena, the roles and mechanisms of organized clouds are not well understood (Neelin et al. 2008; Sherwood et al. 2010; Bony et al. 2015; Mauritsen and Stevens 2015; Reed and Medeiros 2016; Sherwood et al. 2020). Recently, convective self-aggregation (CSA), the spontaneous clustering of convective clouds, has attracted attention because it directly affects climate systems (Held et al. 1993; Tompkins and Craig 1998; Bretherton et al. 2005; Wing et al. 2017). However, a comprehensive theoretical understanding of its mechanism has not yet been developed, and its relationship with real atmospheric phenomena is not yet understood (Muller et al. 2022).

CSA theory should encompass the following features, which have been revealed mainly through numerical studies using complex models:

1. The system has two states: a scattered state in which clouds are randomly generated in a uniform field and an aggregated state in which the dry descending clear area and moist ascending cloudy area are separated.
2. A critical domain size of a few hundred kilometers exists for the onset, below which the state is scattered and above which the state is aggregated (Muller and Held 2012; Jeevanjee and Romps 2013; Yanase et al. 2020).
3. The inter-cluster distance has a characteristic length of a few thousand kilometers, and a structure of that length is selected in a sufficiently large region (Wing and Cronin 2016; Patrizio and Randall 2019; Matsugishi and Satoh 2022; Yanase et al. 2022a).
4. Physical feedback between thermodynamics and dynamics, such as water vapor, clouds, radiation, surface flux, and circulation play a role. (However, which of these feedbacks is essential is a matter of debate, and it is also considered to depend on external environments, e.g., sea surface temperature; Coppin and Bony 2015; Wing et al. 2020; Yanase et al. 2022b).

Several studies have attempted to understand CSA using simple models. Two representative examples are the reaction–diffusion model (Craig and Mack 2013; Windmiller and Craig 2019), which describes the time evolution of the water vapor field, and the gravity wave model (Yang 2021), which incorporates a mass source mimicking radiative cooling and a mass sink mimicking convective heating in a shallow water equation system. Studies based on the water vapor reaction–diffusion model have focused on a coarsening process, highlighting the importance of bistable potentials in the reaction terms and the existence of diffusion. However, it does not exhibit the

coexistence of multiple clusters because the model has no mechanism that determines the typical scale of cloud clusters. Moreover, they do not exhibit advection effects and cannot handle dynamic interactions. Hence, the reaction–diffusion model lacks the abovementioned third and fourth properties. On the other hand, the study based on the gravity wave model points out that the spatial scale of the adjustment of the atmospheric circulation field due to gravity waves (e.g., Bretherton and Smolarkiewicz 1989) plays a role in the scale selection of the CSA. However, thermodynamic interactions cannot be handled. Hence, the gravity wave model lacks the fourth property.

Can we build a unified model that incorporates the best of both models and compensates for their deficiencies? We focused on the water vapor reaction–diffusion–advection model (Ahmed and Neelin 2019, AN19), a water vapor reaction–diffusion model variant. Although the primary purpose of AN19 was to explain the size distribution of tropical mesoscale convection systems, it also reported the occurrence of CSA under certain conditions. However, they did not explain the mechanism of CSA onset nor the horizontal scales. The strength of the AN19 model is its feedback between thermodynamics and dynamics through the coupling of heating and circulation fields while maintaining the time evolution equation of water vapor at its core. However, the heating–circulation coupling in the AN19 model is formulated in the extreme form of "global coupling," in which a point and the entire region are equally coupled. In the context of the gravity wave model, this implies that the effect of gravity waves extends instantaneously over an infinite distance. The scaling proposed by Yang (2021) predicts that the spatial scale of the CSA diverges to infinity. Conversely, we speculate that changing the heating–circulation coupling in the AN19 model to a more natural and general form of "nonlocal coupling" in which the coupling strength between one point and another depends on the distance (e.g., Shima and Kuramoto 2004) would allow scale selection of a finite CSA.

In this study, we investigated how CSA occurs by examining the extended nonlocally coupled AN19 equation in more detail, both theoretically and numerically. In particular, we address whether the wavelength of the CSA can be infinitely extended in a globally coupled system and whether a change to a nonlocally coupled system leads to the selection of a specific wavelength through numerical experiments for the extended AN19 equation and stability analysis of the uniform state. Through this analysis, we propose a unified understanding of the occurrence and scale selection of CSA by combining the essential aspects of both the water vapor reaction–diffusion model and the gravity wave model frameworks. In addition, extending the AN19 equation to CSA theory has implications for understanding the Madden–Julian oscillation (MJO) and water vapor variability in a natural tropical atmosphere. The AN19 model shares a common basis with the moisture mode theory (Sobel and Maloney 2012,2013), which is one of the leading theories of the MJO, and attempts have been made to compare the nature of water vapor variability between actual and ideal atmospheres based on a similar equation (Beucler et al. 2019). In the last part of this paper, we discuss the relationship between our theory and these studies.

Nonlocally coupled moisture model

This study mainly used the time evolution equation of the horizontally extended field of the vertically integrated water vapor content q_v . This is based on the system of equations constructed by AN19 with some simplifications and extensions. Details of the derivation and assumptions are provided in Supporting Information. The set of equations is

$$\frac{\partial q_v}{\partial t} = E - \mathcal{P} + M_q(\nabla \cdot \mathbf{v})q_v + M_q(\mathbf{v} \cdot \nabla)q_v + D\nabla^2 q_v, \quad (1)$$

$$\nabla \cdot \mathbf{v} = \frac{L_v(\mathcal{P} - \tilde{\mathcal{P}}) + (\mathcal{F}_{\text{rad}} - \tilde{\mathcal{F}}_{\text{rad}}) - \xi}{M_s}, \quad (2)$$

where E is the evaporation rate constant; D is the eddy diffusion coefficient constant; M_q is the gross moisture stratification constant; M_s is the gross dry stability constant, and L_v is the latent heat constant. The \mathbf{v} is the horizontal divergent wind vector in the upper troposphere. The vertical structures of the wind field and water vapor content were prescribed. The expression \tilde{A} is the filtered value of a variable A as defined, $\tilde{A}(x) = \int_{-\infty}^{\infty} G(r)A(x+r)dr$, where $G(r)$ is a filter function. For simplicity, we used a box filter $G(r) = \mathcal{H}(l_B/2 - |r|)/l_B$, where l_B denotes the filter length and

$\mathcal{H}(A)$ is the Heaviside step function of a variable A such that $\mathcal{H}(A) = 0$ for $A \leq 0$ and $\mathcal{H}(A) = 1$ for $A > 0$. The above formulation defines the system as a nonlocally coupled system in general. In special cases, this is called a globally coupled system when l_B is infinite or equal to the domain size. The precipitation term \mathcal{P} and column radiative heating term \mathcal{F}_{rad} were parameterized as follows:

$$\mathcal{P} = \alpha(q_v - q_c)\mathcal{H}(q_v - q_c), \quad (3)$$

$$\mathcal{F}_{\text{rad}} = \epsilon_r q_v + \text{const.}, \quad (4)$$

where α is the coefficient of relaxation by precipitation, q_c is the critical water vapor content (the prescribed value is 40 kg m^{-2} in this study). The ϵ_r is the coefficient of water vapor radiative effect. The stochastic term ξ is treated as the Ornstein–Uhlenbeck process (Gardiner 2004):

$$d\xi = -\tau_{\text{noise}}^{-1}\xi dt + \tau_{\text{noise}}^{-1}\sigma_{\text{noise}}dW(t),$$

where τ_{noise} is the damping time scale, σ_{noise} is the intensity of variability, and $dW(t)$ is the Wiener process.

Formally, the system is viewed as being composed of a reaction term \mathcal{R} , advection term \mathcal{A} , diffusion term \mathcal{D} , and stochastic term \mathcal{X} :

$$\begin{aligned} \frac{\partial q_v}{\partial t} &= \mathcal{R} + \mathcal{A} + \mathcal{D} + \mathcal{X}, \\ \mathcal{R} &= E - \mathcal{P} + M_q \frac{L_v(\mathcal{P} - \tilde{\mathcal{P}}) + \epsilon_r(q_v - \tilde{q}_v)}{M_s} q_v, \\ \mathcal{A} &= M_q(\mathbf{v} \cdot \nabla)q_v, \\ \mathcal{D} &= D\nabla^2 q_v, \\ \mathcal{X} &= -\frac{M_q}{M_s}\xi q_v. \end{aligned}$$

Note that the \mathcal{R} is a function of both the local value (q_v) and filtered value ($\tilde{q}_v, \tilde{\mathcal{P}}$). Therefore, we refer to this model as a nonlocally coupled moisture model.

Before discussing the entire system, let us grasp the basic properties without horizontal interaction (i.e., \mathcal{A} and \mathcal{D}) and stochasticity (\mathcal{X}) to focus on the equilibrium states that can be achieved by a local atmospheric column driven only by \mathcal{R} . Fig. 1 shows a bifurcation diagram representing the local equilibrium point of q_v when the \tilde{q}_v is considered a controlled parameter. Here, we assumed $\tilde{\mathcal{P}} = E$. As can be seen from the bifurcation of the local equilibrium point of q_v with respect to the change in \tilde{q}_v in the displayed range, this system can be in a bistable state; that is, two stable solutions coexist for a specific range of \tilde{q}_v . Note that the intersection of the solid line and the line of $q_v = \tilde{q}_v$ in Fig. 1 indicates the existence of a linearly stable horizontally uniform solution in the original spatially extended system. The uniform solution q_{v0} is given by

$$q_{v0} = q_c + \frac{E}{\alpha},$$

where precipitation and evaporation are balanced in each column, that is $P = E$. The growth rate σ for the linear perturbation about the uniform state is

$$\sigma = -\alpha + \frac{M_q}{M_s}q_{v0}(L\alpha + \epsilon_r)(1 - \hat{G}(k)) - Dk^2,$$

where k is the horizontal wavenumber and $\hat{G}(k)$ is the transfer function defined as $\hat{G}(k) = \int_{-\infty}^{\infty} G(r)e^{ikr} dr$. When a box filter is used, $\hat{G}(k) = \sin(kl_B/2)/(kl_B/2)$. Since $\sigma < 0$ for the parameters in this study, the uniform state is linearly stable.

The question is whether this uniform solution, when subjected to a finite-amplitude disturbance, remains in a uniform state (i.e., a scattered state) or transitions to an aggregated state in which two stable solutions (dry and moist) are realized and if it transitions, what wavelength is selected? In the next section, we address this problem using numerical experiments and theoretical considerations of the extended AN19 model.

Self-aggregation in globally and nonlocally coupled systems

First, we conduct a series of numerical experiments on the time evolution of the extended AN19 model in a 1D spatial domain under periodic lateral boundary conditions. We compared the global

coupling runs with different domain sizes and nonlocal coupling runs with different filter lengths. The initial condition is a horizontally uniform field with $q_v = 45 \text{ kg m}^{-2}$. The time integration period was 500 or 1000 days. Fig. 2 shows the space-time distribution of q_v obtained from numerical experiments. As shown in Fig. 2a, for the global coupling run in the 640 km domain, q_v field remained nearly uniform, that is, a scattered state in which precipitation occurred everywhere. When the domain size increased, the q_v field separated into single dry and moist regions, that is, the system transitioned to an aggregated state (Figs. 2b and 2c). For the global coupling system, the horizontal distance between the moist clusters associated with CSA increased as the domain size increased. If the domain size is increased to infinity, it is unknown whether the inter-cluster distance would also increase to infinity. Because it is difficult to determine the system's behavior at infinite domain sizes through numerical experiments, we discuss the structure when there are no domain constraints mathematically from the viewpoint of the bifurcation of dynamical systems later in this paper. In contrast, multiple moist clusters coexisted in the nonlocal coupling runs, as shown in Figs. 2d–f. The horizontal distance between moist clusters increased as the filter length increased.

We now consider why specific wavelengths are selected for nonlocally coupled systems in terms of the stability of the uniform solution. As a uniform solution is linearly stable, it is necessary to consider the effects of finite-amplitude disturbances. Here, we focus on the nonlinearity of the precipitation term, which appears because of the Heaviside function when considering significant drying anomalies from a uniform solution. We propose that when q_v given the (drying) perturbation q'_v from q_{v0} falls below q_c ,

$$q'_v = q_v - q_{v0} < q_c - q_{v0},$$

to change the precipitation effect α to the effective precipitation effect,

$$\alpha_{\text{eff}} = \alpha \frac{(q_{v0} - q_c)}{\Delta q_v},$$

where $\Delta q_v = |q'_v|$ is the absolute value of dry perturbation. By using α_{eff} , an effective growth rate can be newly defined,

$$\sigma_{\text{eff}} = -\alpha_{\text{eff}} + \frac{M_q}{M_s} q_{v0} (L\alpha_{\text{eff}} + \epsilon_r) (1 - \hat{G}(k)) - Dk^2.$$

Fig. 3a shows the effective growth rate as a function of the wavenumber for the globally coupled and nonlocally coupled systems with two different l_B values, assuming a 10240-km domain. Here, we assumed $\Delta q_v = 1 \text{ kg m}^{-2}$. Contributions from precipitation (first term on the r.h.s. of σ_{eff} definition above), divergence term (second term), and diffusion (third term) are shown as well. In a globally coupled system, the effective growth rate has its maximum positive value at the longest wavelength of 10240 km (i.e., the smallest wavenumber) and decreases as the wavelength decreases (i.e., the wavenumber increases). Because the divergence and precipitation terms do not change with the wavenumber, the change in the effective growth rate is caused by diffusion. In the nonlocally coupled system with the 2560-km filter, the effective growth rate has a maximum positive value at an intermediate wavelength of 2048 km. The difference from a globally coupled system is caused by the longwave cutoff of the divergence term owing to nonlocal coupling. With the 640-km filter, the effective growth rate is negative at all wavelengths because the diffusion term dominates. Fig. 3b shows the effective growth rate as a function of filter length and wavelength. The wavelength with the maximum growth rate for a given filter length and the results obtained from the numerical experiments using the extended AN19 model are also shown. The positive effective growth rate region is generally limited to wavelengths smaller than the filter length and larger than approximately 1000 km. The former condition is mainly due to the longwave cutoff caused by nonlocal coupling, and the latter condition is mainly due to diffusion proportional to the square of the wavenumber. The position of the maximum effective growth rate agreed well with the results obtained from the numerical experiments using the extended AN19 model with full nonlinearity. Physically, the filter scale reflects the spatial scale at which the gravity wave adjustment is effective, and this scale should be provided as an external parameter in our model. If we assume the horizontal propagation speed of the first baroclinic mode to be 50 m s^{-1} (Ruppert and Hohenegger 2018) and the damping time scale to be one day (Yang 2021, 2018), the horizontal

length scale as the product is approximately 4000 km. At this filter scale, the maximum effective growth rate wavelength was approximately 3000 km. This scale agrees well with the results of Yanase et al. (2022a), who used a complex cloud-resolving model and found that the characteristic distance of CSA was 3000–4000 km. In addition, we confirmed that the wavelength with the maximum effective growth rate can be obtained even when a Gaussian filter is used and that a spatial structure with such a wavelength is selected in the numerical experiment, although a box filter is used in this study.

Finally, we investigated the reason for the infinite distance in the globally coupled system to underscore the necessity of nonlocal coupling for the finite inter-cluster distance. To understand the characteristics of the horizontal scale of a globally coupled system, we must obtain the spatial distribution of the steady states while retaining the nonlinearity of AN19 and eliminating the effect of the finite domain size. To this end, we analyzed a dynamical system that describes the spatial evolution of state variables and their periodic solutions. The steady state of the 1D globally coupled extended AN19 model can be expressed as

$$\begin{aligned}\frac{dq_v}{dx} &= w \\ \frac{dw}{dx} &= \frac{-\mathcal{R} - M_q u w}{D} \\ \frac{du}{dx} &= \frac{L_v(\mathcal{P} - \bar{\mathcal{P}}) + \epsilon_r(q_v - \bar{q}_v)}{M_s}\end{aligned}$$

where w is the horizontal gradient of q_v , and the u is the horizontal wind velocity. \bar{A} is the horizontal average value of variable A . Here, we assume $\bar{\mathcal{P}} = E$. A trajectory (i.e., spatial distribution) is calculated by integrating the dynamical system for the horizontal dimension x . Periodic trajectories can be found for the appropriate initial conditions. To systematically trace a periodic trajectory and its bifurcation with a change in a parameter (i.e., \bar{q}_v), we used a mathematical method called numerical continuation, which was implemented in the widely used software XPPAUT (Ermentrout and Mahajan 2003; Gandy and Nelson 2022).

For a branch of solutions tracked from a periodic trajectory, the changes in the wavelength (i.e., the distance between the moist clusters) and the minimum and maximum values of the three state variables with \bar{q}_v are shown in Fig. 4. The steady-state results obtained from numerical experiments on the time-dependent problem of the 1D globally coupled extended AN19 model are also shown. For convenience, let $\bar{q}_v = 20 \text{ kg m}^{-2}$ be the starting point and consider first the wavelength (Fig. 4a). As \bar{q}_v increases from 20 kg m^{-2} , the wavelength decreases until $\bar{q}_v \approx 36 \text{ kg m}^{-2}$ and, above that, asymptotically increases to infinity while approaching to $\bar{q}_v = q_{v0}$ (i.e., uniform solution). As \bar{q}_v decreases from 20 kg m^{-2} , the wavelength increases until $\bar{q}_v \approx 14 \text{ kg m}^{-2}$. The branch folds back at $\bar{q}_v \approx 14 \text{ kg m}^{-2}$, and the wavelength asymptotically increases to infinity while approaching to $\bar{q}_v \approx 16 \text{ kg m}^{-2}$. The results of the time-evolving numerical experiments generally agreed with the solution branch obtained from the numerical continuation of the periodic trajectories of the dynamical system. Next, the minimum and maximum of q_v is considered (Fig. 4b). As \bar{q}_v increased from 20 kg m^{-2} , the q_v -max decreased asymptotically to $q_v = q_{v0}$ while approaching to $\bar{q}_v = q_{v0}$. As \bar{q}_v decreases from 20 kg m^{-2} , the q_v -max increases until $\bar{q}_v \approx 14 \text{ kg m}^{-2}$. The branch folds back at $\bar{q}_v \approx 14 \text{ kg m}^{-2}$, and the q_v -max asymptotically increases to the upper stable fixed point of reaction term while approaching to $\bar{q}_v \approx 16 \text{ kg m}^{-2}$. As \bar{q}_v increases from 20 kg m^{-2} , the q_v -min asymptotically increases to $q_v \approx 39 \text{ kg m}^{-2}$ while approaching to $\bar{q}_v = q_{v0}$. As \bar{q}_v decreases from 20 kg m^{-2} , after the branch folds back at $\bar{q}_v \approx 14 \text{ kg m}^{-2}$, the q_v -min asymptotically increases to the unstable fixed point of reaction term while approaching to $\bar{q}_v \approx 16 \text{ kg m}^{-2}$.

At $\bar{q}_v = q_{v0}$, the periodic trajectory asymptotically approaches a single fixed point, corresponding to a uniform solution. This is a homoclinic bifurcation (or saddle-loop bifurcation), a type of infinite-period bifurcation (Strogatz 2019). On the other hand, at $\bar{q}_v \approx 16 \text{ kg m}^{-2}$, the periodic trajectory asymptotically approaches the two fixed points in the phase plane of q_v and w because w asymptotically approaches to zero (Fig. 4d), and these points satisfy $dq_v/dx = 0$ and $dw/dx = 0$. The divergence of u from infinity (Fig. 4c) was consistent with this view. This is a heteroclinic bifurcation. In summary, the wavelength can be infinitely long in a globally coupled system;

conversely, we must use a nonlocally coupled system to allow the finite-scale selection of wavelengths.

Concluding Discussion

The present study proposes a nonlocally coupled moisture model that captures the nature of the onset of CSA and the wavelength selection. Linearly stable uniform states can be destabilized by finite amplitude disturbances. For CSA to occur, the destabilizing effect of feedback due to moisture–heating–circulation coupling must exceed the stabilizing effect of diffusion, which requires that the maximum wavelength, i.e., the domain size for globally coupled systems, is larger than about 1000 km. While the original globally coupled system has the maximum effective growth rate at the longest wavelength, the newly proposed nonlocally coupled system has the maximum effective growth rate approximately at the filter length scale. In globally coupled systems, the wavelength can be infinitely extended because the periodic trajectories in the dynamical system describing the spatial evolution asymptotically approach a heteroclinic trajectory connecting two equilibrium solutions in moist and dry states.

Based on the present theory, how can the CSA be linked to real tropical atmospheric phenomena? In this final section, we discuss the relationship between our theory, the moisture mode theory of MJO, and water vapor variability in the tropical atmosphere. Sobel and Maloney (2012) analyzed the east-west propagating and growing moisture modes along the equator and found that the westward mode with the maximum growth rate appeared at a wavelength of 5000 km, mainly because of surface flux feedback. It is pointed out that the instability is caused by the asymmetry of the precipitation–wind response function and that the east-west wavelength depends on the characteristic scale of the precipitation–wind response function. Furthermore, Sobel and Maloney (2013) reported the existence of an eastward-growing mode with a maximum growth rate at a wavelength of 40000 km, where modes with a scale of a few thousand kilometers were damped by additional terms, such as synoptic disturbance effects, which were not included in Sobel and Maloney (2012). The detailed mechanisms of the present moisture model and their model may differ because they attributed the wind speed dependence of surface fluxes and the east-west asymmetry of the precipitation–wind response function to destabilizing factors, which were not included in our model. However, as Windmiller and Craig (2019) pointed out based on the scaling argument, even if the specific feedback processes that change moisture are different, there will be some commonality in spatial-temporal development. Surface flux feedback can be easily incorporated into our model, and we will address how this affects the CSA mechanism in future studies. Notably, the precipitation-wind response function in their model was formally a nonlocal coupling, which is consistent with our finding that this is important for scale selection. Beucler et al. (2019) compared the spatial variability of moisture between radiative–convective equilibrium experiments in which CSA occurred, a near-global experiment incorporating more realistic equatorial atmospheric dynamics, and a reanalysis data corresponding to the real atmosphere. Their analysis noted that vertical advection may have amplified the spectral peak at several thousand kilometers in the CSA. This is consistent with the fact that the divergence term is the main factor destabilizing the uniform state in our model. The absence of peaks corresponding to the CSA in the near-global experiment and real atmospheric spectra may be due to the effects of the east-west asymmetry of waves and synoptic disturbances, as pointed out by Sobel and Maloney (2012,2013). Taken together, we provide the new insight that CSA can be understood as an ideal form of tropical moisture organization in which synoptic disturbances and zonal asymmetries associated with equatorial atmospheric dynamics are removed from the picture of MJO based on moisture mode theory.

Acknowledgments

The authors thank Yoshiyuki Kajikawa, Yuta Kawai, and Hiroaki Miura for insightful discussions. This study was partly supported by JSPS KAKENHI Grant Number JP24K17128. T.Y. received support from the RIKEN Special Postdoctoral Researcher Program.

References

1. F. Ahmed, J. D. Neelin, Explaining Scales and Statistics of Tropical Precipitation Clusters with a Stochastic Model. *Journal of the Atmospheric Sciences* **76**, 3063–3087 (2019).
2. T. Beucler, T. H. Abbott, T. W. Cronin, M. S. Pritchard, Comparing Convective Self-Aggregation in Idealized Models to Observed Moist Static Energy Variability Near the Equator. *Geophys. Res. Lett.* **46**, 10589–10598 (2019).
3. S. Bony, *et al.*, Clouds, circulation and climate sensitivity. *Nature Geosci* **8**, 261–268 (2015).
4. C. S. Bretherton, P. N. Blossey, M. Khairoutdinov, An Energy-Balance Analysis of Deep Convective Self-Aggregation above Uniform SST. *Journal of the Atmospheric Sciences* **62**, 4273–4292 (2005).
5. C. S. Bretherton, P. K. Smolarkiewicz, Gravity Waves, Compensating Subsidence and Detrainment around Cumulus Clouds. *J. Atmos. Sci.* **46**, 740–759 (1989).
6. D. Coppin, S. Bony, Physical mechanisms controlling the initiation of convective self-aggregation in a General Circulation Model. *J. Adv. Model. Earth Syst.* **7**, 2060–2078 (2015).
7. G. C. Craig, J. M. Mack, A coarsening model for self-organization of tropical convection. *J. Geophys. Res. Atmos.* **118**, 8761–8769 (2013).
8. B. Ermentrout, *Simulating, Analyzing, and Animating Dynamical Systems* (Society for Industrial and Applied Mathematics, 2002).
9. D. L. Gandy, M. R. Nelson, Analyzing Pattern Formation in the Gray–Scott Model: An XPPAUT Tutorial. *SIAM Rev.* **64**, 728–747 (2022).
10. C. W. Gardiner, *Handbook of Stochastic Methods*.
11. I. M. Held, R. S. Hemler, V. Ramaswamy, Radiative-Convective Equilibrium with Explicit Two-Dimensional Moist Convection. *J. Atmos. Sci.* **50**, 3909–3927 (1993).
12. N. Jeevanjee, D. M. Romps, Convective self-aggregation, cold pools, and domain size. *Geophys. Res. Lett.* **40**, 994–998 (2013).
13. S. Matsugishi, M. Satoh, Sensitivity of the Horizontal Scale of Convective Self-Aggregation to Sea Surface Temperature in Radiative Convective Equilibrium Experiments Using a Global Nonhydrostatic Model. *Journal of Advances in Modeling Earth Systems* **14**, e2021MS002636 (2022).
14. T. Mauritsen, B. Stevens, Missing iris effect as a possible cause of muted hydrological change and high climate sensitivity in models. *Nature Geosci* **8**, 346–351 (2015).
15. C. J. Muller, I. M. Held, Detailed Investigation of the Self-Aggregation of Convection in Cloud-Resolving Simulations. *Journal of the Atmospheric Sciences* **69**, 2551–2565 (2012).
16. C. Muller, *et al.*, Spontaneous Aggregation of Convective Storms. *Annu. Rev. Fluid Mech.* **54**, 133–157 (2022).

17. J. D. Neelin, O. Peters, J. W.-B. Lin, K. Hales, C. E. Holloway, Rethinking convective quasi-equilibrium: observational constraints for stochastic convective schemes in climate models. *Phil. Trans. R. Soc. A* **366**, 2579–2602 (2008).
18. C. R. Patrizio, D. A. Randall, Sensitivity of Convective Self-Aggregation to Domain Size. *J. Adv. Model. Earth Syst.* **11**, 1995–2019 (2019).
19. K. A. Reed, B. Medeiros, A reduced complexity framework to bridge the gap between AGCMs and cloud-resolving models. *Geophys. Res. Lett.* **43**, 860–866 (2016).
20. J. H. Ruppert, C. Hohenegger, Diurnal Circulation Adjustment and Organized Deep Convection. *J. Climate* **31**, 4899–4916 (2018).
21. S. C. Sherwood, R. Roca, T. M. Weckwerth, N. G. Andronova, Tropospheric water vapor, convection, and climate. *Rev. Geophys.* **48**, RG2001 (2010).
22. S. C. Sherwood, *et al.*, An Assessment of Earth's Climate Sensitivity Using Multiple Lines of Evidence. *Rev. Geophys.* **58** (2020).
23. S. Shima, Y. Kuramoto, Rotating spiral waves with phase-randomized core in nonlocally coupled oscillators. *Phys. Rev. E* **69**, 036213 (2004).
24. A. P. Siebesma, S. Bony, C. Jakob, B. Stevens, Eds., *Clouds and Climate: Climate Science's Greatest Challenge* (Cambridge University Press, 2020).
25. A. Sobel, E. Maloney, An Idealized Semi-Empirical Framework for Modeling the Madden-Julian Oscillation. *Journal of the Atmospheric Sciences* **69**, 1691–1705 (2012).
26. A. Sobel, E. Maloney, Moisture Modes and the Eastward Propagation of the MJO. *Journal of the Atmospheric Sciences* **70**, 187–192 (2013).
27. S. H. Strogatz, *Nonlinear Dynamics and Chaos: With Applications to Physics, Biology, Chemistry, and Engineering*, 2nd Ed. (CRC Press, 2019).
28. A. M. Tompkins, G. C. Craig, Radiative–convective equilibrium in a three-dimensional cloud-ensemble model. *Q.J. Royal Met. Soc.* **124**, 2073–2097 (1998).
29. J. M. Windmiller, G. C. Craig, Universality in the Spatial Evolution of Self-Aggregation of Tropical Convection. *Journal of the Atmospheric Sciences* **76**, 1677–1696 (2019).
30. A. A. Wing, T. W. Cronin, Self-aggregation of convection in long channel geometry. *Q.J.R. Meteorol. Soc.* **142**, 1–15 (2016).
31. A. A. Wing, K. Emanuel, C. E. Holloway, C. Muller, Convective Self-Aggregation in Numerical Simulations: A Review. *Surv Geophys* **38**, 1173–1197 (2017).
32. A. A. Wing *et al.*, Clouds and Convective Self-Aggregation in a Multimodel Ensemble of Radiative-Convective Equilibrium Simulations. *J Adv Model Earth Syst* **12** (2020).
33. T. Yanase, S. Nishizawa, H. Miura, T. Takemi, H. Tomita, New critical length for the onset of self-aggregation of moist convection. *Geophysical Research Letters* **47**, e2020GL088763 (2020).
34. T. Yanase, S. Nishizawa, H. Miura, H. Tomita, Characteristic Form and Distance in High-Level Hierarchical Structure of Self-Aggregated Clouds in Radiative-Convective Equilibrium. *Geophysical Research Letters* **49**, e2022GL100000 (2022a).

35. T. Yanase, S. Nishizawa, H. Miura, T. Takemi, H. Tomita, Low-Level Circulation and Its Coupling with Free-Tropospheric Variability as a Mechanism of Spontaneous Aggregation of Moist Convection. *Journal of the Atmospheric Sciences* **79**, 3429–3451 (2022b).
36. D. Yang, Boundary Layer Height and Buoyancy Determine the Horizontal Scale of Convective Self-Aggregation. *Journal of the Atmospheric Sciences* **75**, 469–478 (2018).
37. D. Yang, A Shallow-Water Model for Convective Self-Aggregation. *Journal of the Atmospheric Sciences* **78**, 571–582 (2021).

Figures and Tables

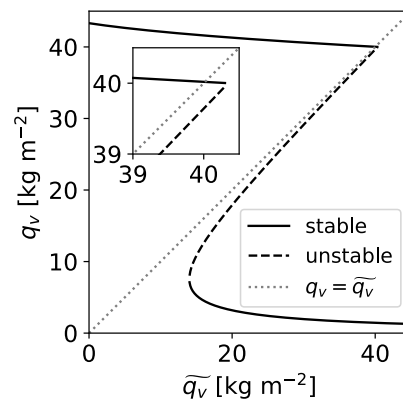


Figure 1. Bifurcation diagram of q_v against \bar{q}_v . Solid (dashed) lines represent stable (unstable) fixed points. Dotted line represents $q_v = \bar{q}_v$. The water balance $\bar{P} = E$ is assumed.

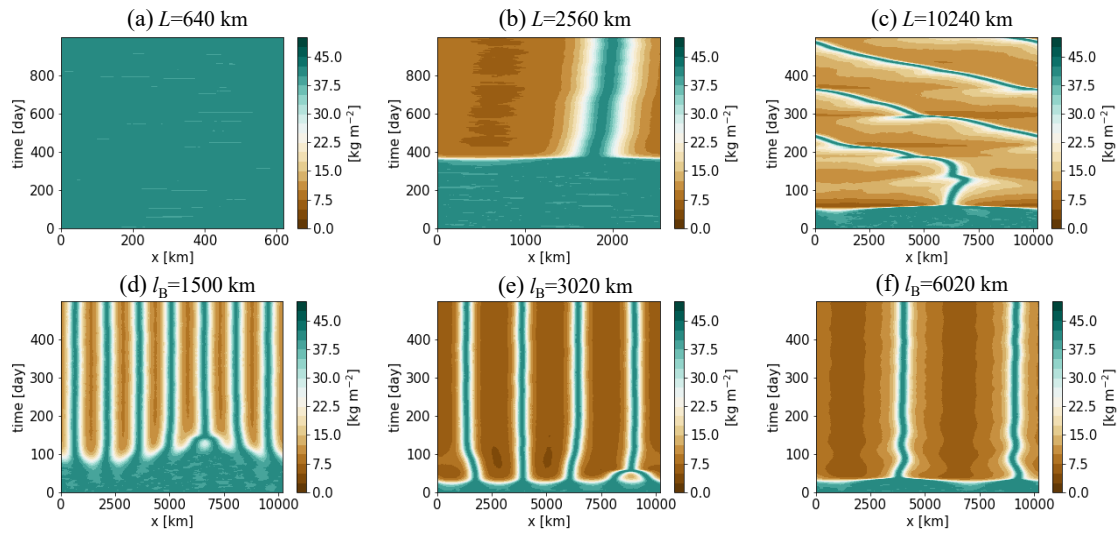


Figure 2. Space–time distribution of q_v . (a)–(c) Global coupling runs on 640-, 2560-, and 10240-km domains. (d)–(f) Nonlocal coupling runs with 1500-, 3020-, and 6020-km filter lengths on the 10240-km domain.

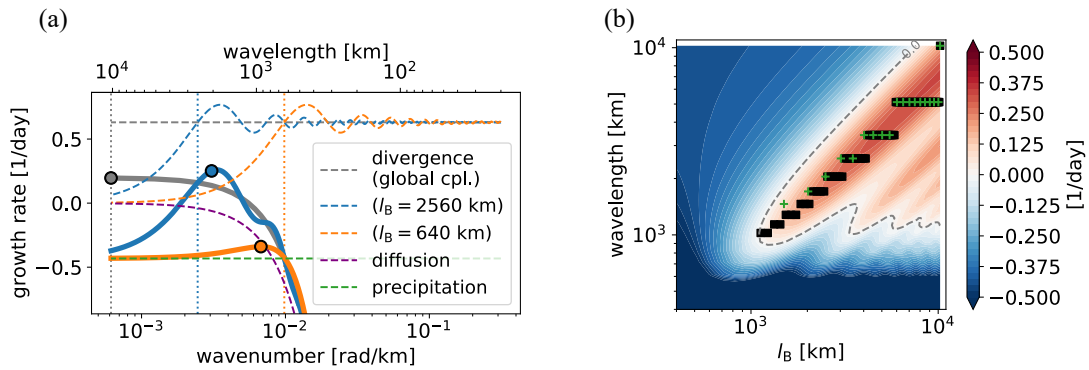


Figure 3. Effective growth rate as a function of wavenumber and l_B . The perturbation Δq_v is assumed to be 1 kg m^{-2} . (a) Effective growth rate and contribution from each term against the horizontal wavenumber. Gray, blue, and orange solid line represents the effective growth rate for the globally coupled system and the nonlocally coupled system with $l_B = 2560, 640 \text{ km}$, respectively. Divergence terms are represented by dashed lines colored the same as the effective growth rate. Green and purple dashed lines represent the precipitation and the diffusion term, respectively. Circles on the solid lines represent the maximum effective growth rate among the discrete modes for the periodic domain with the size of 10240 km . Vertical dotted lines represent l_B . Wavelength is shown at the horizontal axis on the top. (b) Effective growth rate in l_B -wavelength space. Black squares are the points with maximum effective growth rate at a given l_B . Green crosses are the results obtained by the numerical experiments of the nonlocally coupled system.

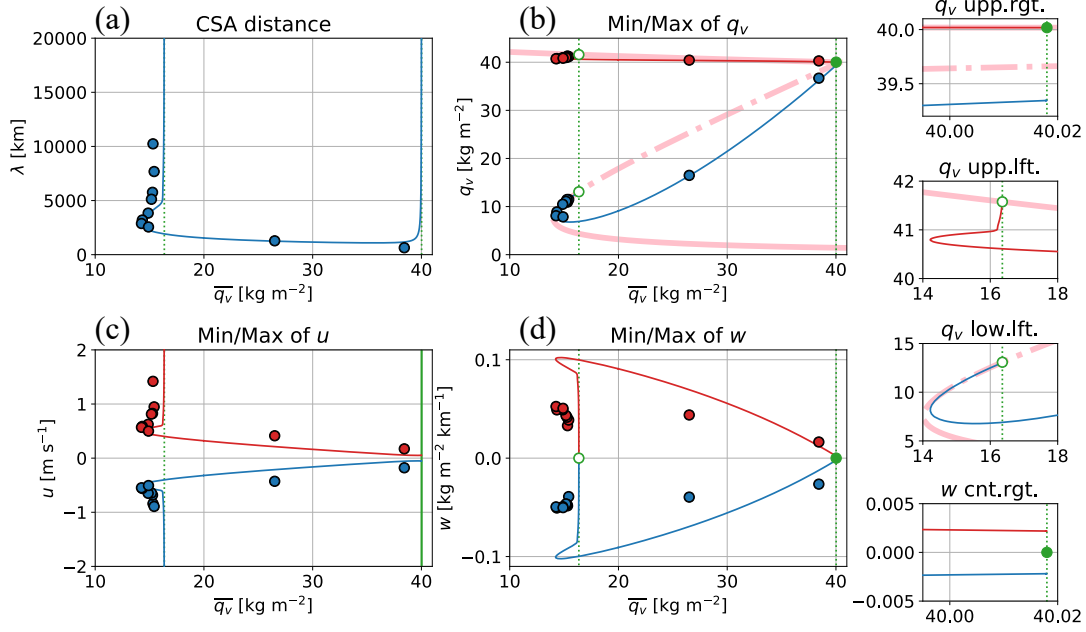


Figure 4. Properties of periodic trajectories of the dynamical system describing the spatial evolution in steady state of globally coupled system against the change in \bar{q}_v . (a) Blue solid line represents the wavelength obtained by the numerical continuation. Blue circles represent the wavelength obtained by the time evolving numerical experiments. (b) Same as (a) except for the red (blue) represents the maximum (minimum) of q_v along the trajectories. (c) Same as (b) except for u . (d) Same as (b) except for w . Pink lines in (b) are the same as black lines in Fig. 1. Green filled circles and solid line are the uniform solution; $q_v = q_{v0}$, $w = 0$, and u can be arbitrary value. Green open circles are the fixed points for the heteroclinic trajectory at $\bar{q}_v \approx 16$ kg m⁻²; q^*_v such that $\mathcal{R}(q^*_v) = 0$, $w = 0$. The rightmost small panels focus on the parts of (b) and (d).

Supporting Information for

Nonlocally coupled moisture model for convective self-aggregation

Tomoro Yanase, Shin-ichiro Shima, Seiya Nishizawa, Hirofumi Tomita

*Tomoro Yanase

Email: tomoro.yanase@riken.jp

This PDF file includes:

Supporting text

Figures S1

Tables S1 to S2

SI References

Supporting Information Text

Basic equations

We follow Ahmed and Neelin (2019). One of the main differences from the original system of equations was the exclusion of water condensate as a prognostic variable and the associated cloud radiative effect. This facilitated a semi-analytical understanding. In addition, the rotational component of horizontal wind was excluded. We made this change because we were interested in the behavior of clouds in nonrotating systems. Other changes were made to the vertical distribution functions and other parameters. A more reproducible analytical expression was used for the vertical distribution functions. Although these parameters may have changed the quantitative results, they did not affect the main conclusions. For example, the changes in the phase diagram for a wide range of parameters can be easily confirmed. In the following section, the specific system of equations is explained. The variables, functions, and parameters used in this study are summarized in Tables S1 and S2.

Mass continuity equation

Mass continuity equation in pressure coordinates is,

$$\frac{\partial \omega}{\partial p} + \nabla \cdot \mathbf{V} = 0, \quad (\text{S1})$$

where $\omega = \omega(x, y, p, t)$ [Pa s^{-1}] is the vertical velocity, p [Pa] is the pressure, and $\mathbf{V} = \mathbf{V}(x, y, p, t)$ [m s^{-1}] is the horizontal velocity vector. We assume that the vertical velocity has a prescribed vertical structure.

$$\omega = -a\Omega_1, \quad (\text{S2})$$

where $a = a(x, y, t)$ [s^{-1}] is the horizontally and temporally varying component, the horizontal divergence in the upper part of the atmosphere, and $\Omega_1 = \Omega_1(p)$ [Pa] is the vertically varying component, the vertical structure function. According to Equations (S1) and (S2)

$$\nabla \cdot \mathbf{V} = \frac{d\Omega_1}{dp} \nabla \cdot \mathbf{v},$$

where $\mathbf{v} = \mathbf{v}(x, y, t)$ [m s^{-1}] is the horizontal divergent wind such that $\nabla \cdot \mathbf{v} = a$. In this study, the vertical structure of vertical velocity is expressed as follows:

$$\Omega_1 = \frac{p_b - p_t}{2} \sin\left(\frac{\pi(p - p_t)}{p_b - p_t}\right),$$

where p_b [Pa] and p_t [Pa] are the pressures at the bottom and top of the atmospheric column (constant), respectively. This is referred to as the first baroclinic mode.

Thermodynamic equation

We consider a vertically integrated dry static energy budget equation. We applied the weak temperature gradient approximation, that is, the local tendency term and horizontal advection term were neglected (Sobel et al. 2001; Sobel and Bretherton 2000; Sobel et al. 2007). Convective and radiative heating were considered for horizontally and temporally varying vertically integrated diabatic heating. The sensible heat flux at the ground surface was assumed to be constant. In addition, a stochastic term is included.

The diagnostic balance equation of dry static energy s [J kg^{-1}] is modeled as

$$\left\langle \omega \frac{ds}{dp} \right\rangle = L_v(\mathcal{P} - \tilde{\mathcal{P}}) + (\mathcal{F}_{\text{rad}} - \tilde{\mathcal{F}}_{\text{rad}}) - \xi,$$

where the lhs is the vertically integrated vertical advection of dry static energy, L_v [$\text{W m}^{-2} \text{kg}^{-1} \text{m}^2 \text{s}$] is the latent heat constant, $\mathcal{P} = \mathcal{P}(q_v)$ [$\text{kg m}^{-2} \text{s}^{-1}$] is the surface precipitation rate as a function of vertically integrated water vapor content $q_v = q_v(x, y, t)$, $\mathcal{F}_{\text{rad}} = \mathcal{F}_{\text{rad}}(q_v)$ [W m^{-2}] is the column radiative heating rate as a function of q_v , and $\xi = \xi(x, y, t)$ [W m^{-2}] is the stochastic term by the Ornstein–Uhlenbeck process. Expression $\langle A \rangle$ is the vertical integral of variable A as follows:

$$\langle A \rangle = \frac{1}{g} \int_{p_t}^{p_b} A(p') dp'$$

where g [m s^{-2}] is the gravitational acceleration constant. Expression \bar{A} is the filtered value of variable A (see the main manuscript). We assume that the change in dry static energy with respect to pressure is constant (i.e., $ds/dp = \text{const.}$). By using this specified vertical structure function and integrating the vertical advection term,

$$\nabla \cdot \mathbf{v} = \frac{L_v(\mathcal{P} - \bar{\mathcal{P}}) + (\mathcal{F}_{\text{rad}} - \bar{\mathcal{F}}_{\text{rad}}) - \xi}{M_s}, \quad (\text{S3})$$

where $M_s = (ds/dp)(p_b - p_t)^2/(g\pi)$ is referred to as the gross dry stability. The surface precipitation rate \mathcal{P} is parameterized as a piecewise linear function of q_v

$$\mathcal{P} = \alpha(q_v - q_c)\mathcal{H}(q_v - q_c)$$

where α is the coefficient of relaxation by precipitation, q_c is the critical column water vapor content, and \mathcal{H} is the Heaviside step function such that $\mathcal{H}(A) = 0$ for $A \leq 0$ and $\mathcal{H}(A) = 1$ for $A > 0$. The radiative heating rate \mathcal{F}_{rad} is parameterized as a linear function of q_v

$$\mathcal{F}_{\text{rad}} = \epsilon_r q_v + \text{const.}$$

where ϵ_r [$\text{W m}^{-2} \text{kg}^{-1} \text{m}^2$] is the coefficient of water vapor radiative effect. The stochastic term ξ reflecting the heating variability not included by precipitation and radiation is parameterized by the following stochastic time evolution equation

$$d\xi = -\tau_{\text{noise}}^{-1} \xi dt + \tau_{\text{noise}}^{-1} \sigma_{\text{noise}} dW(t)$$

where τ_{noise} is the damping time scale, σ_{noise} is the intensity of variability, and $dW(t)$ is the Wiener process.

Water vapor equation

We assume that the specific humidity q [kg kg^{-1}] has a prescribed vertical structure,

$$q = q_v \Omega_2,$$

where $q_v = \langle q \rangle$ is the vertically integrated water vapor content and $\Omega_2 = \Omega_2(p)$ [$\text{Pa}^{-1} \text{m s}^{-2}$] expresses the vertical variation of specific humidity:

$$\Omega_2(p) = \frac{g(e^{p/p_q} - e^{p_t/p_q})}{p_q(e^{p_b/p_q} - e^{p_t/p_q}) - e^{p_t/p_q}(p_b - p_t)}$$

where p_q [Pa] is the scale of the pressure for a vertical change in water vapor content. This function form is chosen such that it satisfies $\Omega_2(p_t) = 0$, $\langle \Omega_2 \rangle = 1$, and increasing with pressure exponentially. The prognostic equation of vertically integrated water vapor content q_v is modeled as

$$\frac{\partial q_v}{\partial t} = E - \mathcal{P} + M_q(\nabla \cdot \mathbf{v})q_v + M_q(\mathbf{v} \cdot \nabla)q_v + D\nabla^2 q_v,$$

where E [$\text{kg m}^{-2} \text{s}^{-1}$] is the evaporation rate constant, D [$\text{m}^2 \text{s}^{-1}$] is the eddy diffusion coefficient constant, and $M_q = \langle -\Omega_2 d\Omega_1/dp \rangle$ is referred to as the gross moisture stratification.

In addition, by introducing the velocity potential ϕ such that $\nabla^2 \phi$ equals to the rhs of Equation (S3) and solving the Poisson's equation, the spatial field of \mathbf{v} is determined.

The reaction term defined in the main manuscript is a quadratic function of q_v below q_c and above q_c , respectively. For $q_v \leq q_c$

$$\mathcal{R} = A_1 q_v^2 + B_1 q_v + C_1, \quad (\text{S4})$$

$$A_1 = \frac{M_q}{M_s} \epsilon_r, \quad B_1 = -\frac{M_q}{M_s} (L_v \bar{\mathcal{P}} + \epsilon_r \bar{q}_v), \quad C_1 = E,$$

and for $q_v > q_c$

$$\mathcal{R} = A_2 q_v^2 + B_2 q_v + C_2, \quad (\text{S5})$$

$$A_2 = \frac{M_q}{M_s} (\alpha L_v + \epsilon_r), \quad B_2 = -\left(\alpha + \alpha \frac{M_q}{M_s} L_v q_c + \bar{\mathcal{P}} \frac{M_q}{M_s} L_v + \frac{M_q}{M_s} \epsilon_r \bar{q}_v \right), \quad C_2 = E + \alpha q_c.$$

The potential function is defined as

$$\mathcal{V}(q_v) = -\int_0^{q_v} \mathcal{R}(q_v') dq_v' + \text{const.}$$

where the constant is set such that $\mathcal{V}(q_c) = 0$. Fig. S1 (a) and (b) show examples of the tendency and potential as functions of the column water vapor content for a given radiative coefficient and different average column water vapor content values. Figs S1 (c)–(f) also show the discriminants for the quadratic equations of Equations (S4) and (S5) being zero, respectively, and the solutions $Q_1, Q_2, Q_3,$ and Q_4 , the local equilibrium points, as functions of the average column water vapor content and the radiative coefficient.

Conditions for multiple equilibria

We consider a dynamic system whose time evolution is described only by the reaction term, and show the conditions for a multiple equilibrium state. Because the quadratic function representing the reaction term changes depending on whether q_v is larger or smaller than q_c , we divided the system into cases. The reaction term is a quadratic function that is convex downwards for each range (i.e., $A_1 > 0$ and $A_2 > 0$), and the maximum number of stable solutions is two. Therefore, multiple equilibrium states are bistable.

The condition for the existence of a dry stable solution is that the quadratic equation of Equation (S4) is zero, has two real solutions, Q_1 and $Q_2 (> Q_1)$, and the stable solution Q_1 is within the domain. That is, $B_1^2 - 4A_1C_1 > 0$, and $0 < Q_1 < q_c$.

Similarly, the condition for the existence of a moist stable solution is that, $B_2^2 - 4A_2C_2 > 0$, and $Q_3 > q_c$, where Q_3 and $Q_4 (> Q_3)$ are two real solutions when Equation (S5) is zero.

Time-evolving numerical experiment

In the time-evolving numerical experiments of the fully nonlinear governing equations, spatial discretization was performed based on a horizontal one-dimensional Cartesian coordinate system. Periodic lateral boundary conditions were imposed. The horizontal advection term and horizontal convergence term (the term attributed to the vertical integration of the vertical advection) included in the reaction term are computed simultaneously as the horizontal flux convergence after being combined into the flux form. The velocity vector field was calculated as the first-order spatial derivative of the velocity potential. The scalar field of the velocity potential was calculated by expressing the velocity divergence term in the thermodynamic equation in terms of the second-order spatial derivative of the velocity potential and numerically solving the obtained Poisson equation using the SOR method. The horizontal flux convergence was calculated using the second-order centered difference method after obtaining the value of the horizontal flux at the point horizontally shifted by half a grid from the position of the scalar value. The time evolution of the stochastic term was computed using the Euler–Maruyama method and the Wiener process was represented by a normal random number generated using the Box–Muller method. The horizontal grid size was 20 km and the time interval was 300 s. The horizontal domain size was varied as the control parameter. Initial column water vapor field is uniform value 45 kg m^{-2} plus uniform random numbers with width of 1 kg m^{-2} .

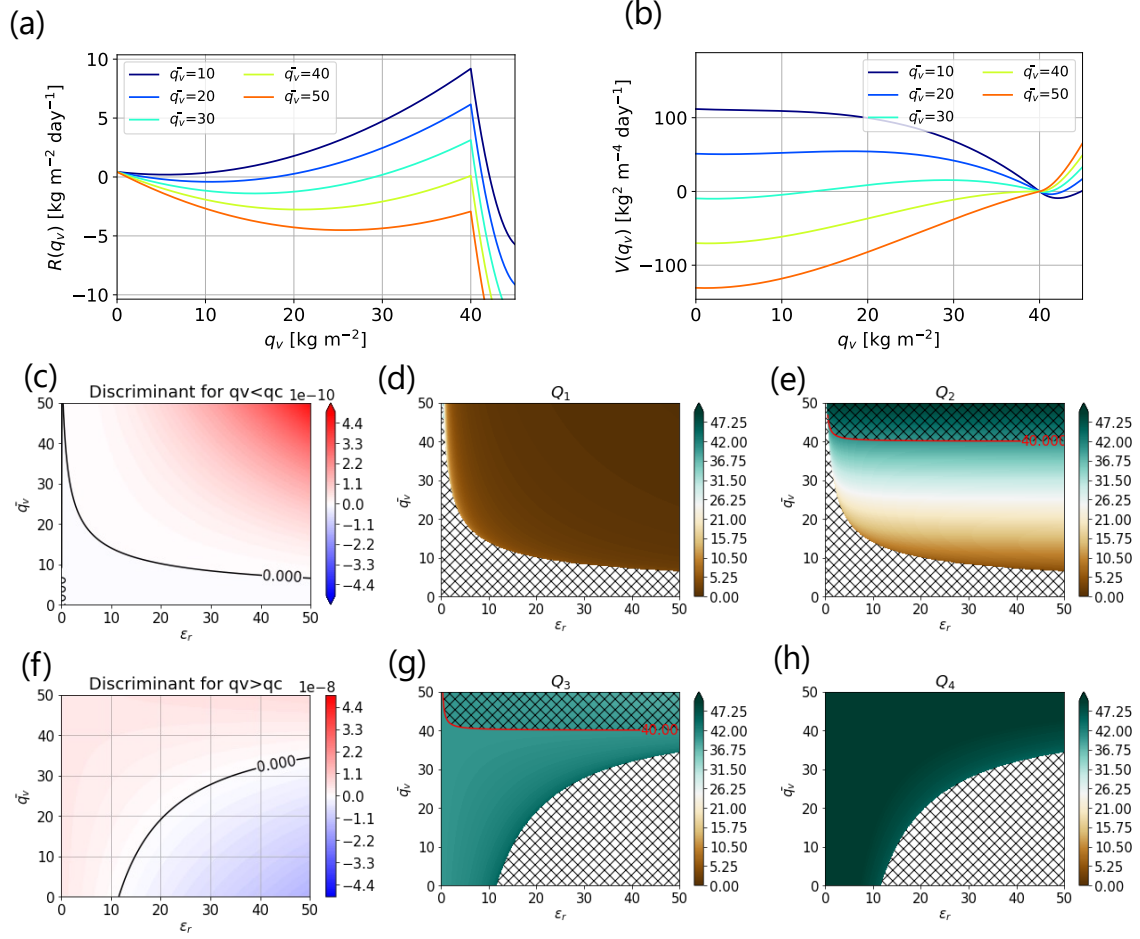


Fig. S1. Characteristics of the reaction term. (a) Tendency by the reaction term and (b) potential function as a function of column water vapor content q_v for various average column water vapor content \bar{q}_v . The case of $\epsilon_r = 10 \text{ W m}^{-2} \text{ kg}^{-1} \text{ m}^2$. (c) Discriminant and (d)–(e) solutions for the quadratic equation of reaction term Eq. (S4) being zero, and (f) discriminant and (g)–(h) solutions for the quadratic equation of reaction term Eq. (S5) being zero, as a function of radiative coefficient (horizontal axis) and average column water vapor content (vertical axis).

Table S1. List of variables and functions.

Symbol	Description	Unit	Note
p	Pressure	Pa	-
ω	Vertical wind velocity	Pa s^{-1}	-
\mathbf{V}	Horizontal wind velocity vector	m s^{-1}	-
\mathbf{v}	Horizontal divergent velocity vector in the upper troposphere	m s^{-1}	-
s	Dry static energy	J kg^{-1}	-
q	Specific humidity	kg kg^{-1}	-
q_v	Column water vapor content	kg m^{-2}	-
ξ	Stochastic heating	W m^{-2}	-
\mathcal{P}	Surface precipitation rate	$\text{kg m}^{-2} \text{s}^{-1}$	Function of q_v
\mathcal{F}_{rad}	Column radiative heating rate	W m^{-2}	Function of q_v
\mathcal{H}	Heaviside step function	-	Function of q_v

Table S2. List of parameters.

Symbol	Description	Value	Note
E	Evaporation rate	$5.0 \times 10^{-6} \text{ kg m}^{-2} \text{ s}^{-1}$	-
D	Eddy diffusion coefficient	$7.5 \times 10^4 \text{ m}^2 \text{ s}^{-1}$	-
M_q	Gross moisture stratification	1.14	$ds/dp = -0.5 \text{ J kg}^{-1} \text{ Pa}^{-1}$
p_q	Pressure scale of water vapor change	20000 Pa	-
M_s	Gross dry stability	$1.3 \times 10^8 \text{ J m}^{-2}$	-
L_v	Latent heat	$2.16 \times 10^6 \text{ W m}^{-2} \text{ kg}^{-1} \text{ m}^2 \text{ s}$	Column heating per precipitation rate
g	Gravitational acceleration	9.81 m s^{-2}	-
p_b	Pressure at the troposphere bottom	100000 Pa	-
p_t	Pressure at the troposphere top	10000 Pa	-
α	Coefficient of water vapor relaxation by precipitation	3600^{-1} s^{-1}	-
q_c	Critical column water vapor content	40 kg m^{-2}	-
ϵ_r	Coefficient of water vapor radiative effect	$10 \text{ W m}^{-2} \text{ kg}^{-1} \text{ m}^2$	-
τ_{noise}^{-1}	Damping time scale of the stochastic process	7200 s	-
σ_{noise}	Amplitude of stochastic forcing	30 W m^{-2}	-

SI References

1. F. Ahmed, J. D. Neelin, Explaining Scales and Statistics of Tropical Precipitation Clusters with a Stochastic Model. *Journal of the Atmospheric Sciences* **76**, 3063–3087 (2019).
2. A. H. Sobel, G. Bellon, J. Bacmeister, Multiple equilibria in a single-column model of the tropical atmosphere. *Geophys. Res. Lett.* **34**, L22804 (2007).
3. A. H. Sobel, C. S. Bretherton, Modeling Tropical Precipitation in a Single Column. *J. Climate* **13**, 4378–4392 (2000).
4. A. H. Sobel, J. Nilsson, L. M. Polvani, The Weak Temperature Gradient Approximation and Balanced Tropical Moisture Waves. *J. Atmos. Sci.* **58**, 3650–3665 (2001).